

**Experimental and Modeling Studies of Two-Phase Flow in Porous  
Media and Its Effects on the Performance of a PEM Fuel Cell**

Xuhai Wang

B.S. Chemical Engineering, Sichuan University, Chengdu, China, 2000

M.S. Chemical Technology, Institute of Process Engineering, Chinese Academy of  
Sciences, Beijing, 2004

Submitted to the graduate degree program in Chemical & Petroleum Engineering and  
the Graduate Faculty of the University of Kansas School of Engineering in partial  
fulfillment of the requirements for the degree of Doctor of Philosophy.

Committee Members:

---

Chairman: Dr. Trung Van Nguyen

---

Dr. Jenn-Tai Liang

---

Dr. Aaron M. Scurto

---

Dr. Peter W. TenPas

---

Dr. Laurence Weatherley

Date of Defense: Jan. 26, 2010

The Dissertation Committee for Xuhai Wang certifies that this is the approval version  
of the following dissertation:

**Experimental and Modeling Studies of Two-Phase Flow in Porous  
Media and Its Effects on the Performance of a PEM Fuel Cell**

Committee Members:

---

Chairman: Dr. Trung V. Nguyen

---

Dr. Jenn-Tai Liang

---

Dr. Aaron M. Scurto

---

Dr. Peter W. TenPas

---

Dr. Laurence Weatherley

Date approved: Jan. 28, 2010

## **Abstract**

An experimental investigation was conducted to study the two-phase flow properties of porous media used in proton exchange membrane (PEM) fuel cells. The liquid and gas phase relative permeability of porous media used in PEM fuel cells was measured at the University of Kansas and validated using the neutron imaging facility at the National Institute of Science and Technology (NIST). New correlations between the liquid saturation levels and relative permeability were identified. These correlations were further used to determine the liquid saturation levels in the electrodes of a PEM fuel cell during operation. The results showed that the 3<sup>rd</sup>-order power correlations between saturation levels and permeability developed for hydrophilic sands were unsuitable for the gas diffusion layers (GDLs) used in PEM fuel cells. The GDLs made of graphite fibers have different surface properties and structures than the well-sorted sands, causing a difference in the two-phase flow properties.

One-dimensional two-phase flow models were developed to study the effect of the porous media on the liquid saturation levels, liquid water management strategies, and fuel cell performance. To address the saturation level discontinuity created at the interface of two materials with different wetting properties, a saturation jump

condition was included in the models. This study showed that the hydrophobic part of the capillary curve was more important than the hydrophilic part because the zero capillary pressure ( $p_c=0$ ) condition at the gas channel/GDL interface bound the liquid saturation levels in the hydrophobic region. The properties of the GDLs affected the fuel cell performances greatly when the reactant transport in the porous media was the limiting step. The model including a micro-porous layer (MPL) in the cathode side showed that the zero-net-water-transport-across-the-membrane was achievable, which would eliminate the anode humidification requirement and improve the fuel cell performance. Hydrophobic catalyst layers (CLs) in the cathode and anode were required to prevent the CLs from being flooded, when the hydrophobic MPL was presented in the cathode side. The complete model consisting of both the cathode and anode showed that the liquid water transport rate from the cathode to the anode was higher when there was no MPL in the anode side. The complete model also showed that when the anode was treated as an interface instead of a complete porous electrode, over-prediction of the fuel cell voltage resulted, mainly from the omission of the ohmic losses in the anode.

## **Acknowledgements**

I would like to express my sincere gratitude to my advisor, Dr. Trung Van Nguyen, who introduced me to this fascinating and rewarding field of study. Dr. Nguyen continuously supported and directed my research and study. He was always available to give me guidance and assistance, even during his two-year service to the National Science Foundation (NSF) in Washington, DC. His mentorship and insight will continue to inspire me both personally and professionally.

I would also like to thank my committee members, Dr. Jenn-Tai Liang, Dr. Aaron M. Scurto, Dr. Peter W. TenPas, and Dr. Laurence Weatherley, for their valuable time, helpful advice and critical review of my dissertation. Thanks also go to Dr. Kyle V. Camarda and Dr. Javier Guzman for serving on my comprehensive exam committee.

My colleagues, Heebong Ohn, Roland Friedmann and Yan Gao, also deserve thanks for their frequent assistance with this experiment. Thanks go to Dr. Qiang Ye for his helpful discussion of fuel cell modeling. I also thank Will Musgrove and Andrea Senf for proofreading my manuscript.

I would like to acknowledge the staff of the Chemical & Petroleum Engineering Department for their services. I thank TVN Systems, Inc. for generously providing

me with an internship and also for supplying fuel cell electrodes, gaskets and other materials for my study. I thank the National Institute of Standards and Technology (NIST) for providing the neutron imaging facility.

And finally, none of this could have been accomplished without the unconditional support of my family over the past years. My special thanks go to my wife, Jing Fang, for her support and patience during my study at KU and to my daughter, Ashley T. Wang, who brings so much happiness to my life.

## Table of Contents

<b>Title Page.....</b>	<b>I</b>
<b>Acceptance Page.....</b>	<b>II</b>
<b>Abstract.....</b>	<b>III</b>
<b>Acknowledgements.....</b>	<b>V</b>
<b>Table of Contents.....</b>	<b>VII</b>
<b>List of Figures.....</b>	<b>XII</b>
<b>List of Tables.....</b>	<b>XIX</b>
<b>List of Symbols.....</b>	<b>XXI</b>
<b>Chapter 1 Introduction.....</b>	<b>1</b>
1.1 Fuel Cell Benefits.....	1
1.2 Fuel Cell Types.....	3
1.3 PEM Fuel Cell Components and Transport.....	7
1.4 PEM Fuel Cell Thermodynamics.....	13
1.5 PEM Fuel Cell Performance.....	16
1.6 Motivation and Objectives.....	18
1.7 References.....	22

<b>Chapter 2 Experimental Study of Relative Permeability of Porous Media Used in PEM Fuel Cells.....</b>	<b>25</b>
2.1 Introduction.....	25
2.2 Experimental.....	28
2.2.1 Materials.....	28
2.2.2 Gas Permeability.....	29
2.2.3 Liquid Permeability.....	34
2.3 Results and Discussion.....	36
2.3.1 Gas Relative Permeability.....	36
2.3.2 Liquid Relative Permeability.....	43
2.4 Conclusions.....	49
2.5 References.....	50
<b>Chapter 3 Experimental Evaluation of Saturation Levels in the Cathode side and Cell Performance of a PEM Fuel Cell.....</b>	<b>54</b>
3.1 Introduction.....	54
3.2 Experimental.....	57
3.2.1 Setup.....	57
3.2.2 Procedure.....	59
3.2.3 Materials.....	61





3.3 Results and Discussion.....	62
3.3.1 Relative Permeability Correlations.....	62
3.3.2 Base Case.....	64
3.3.3 Stoichiometric Effect.....	71
3.3.4 Temperature Effect.....	74
3.4 Conclusions.....	76
3.5 References.....	77
<b>Chapter 4 Modeling the Effects of Capillary Property of Porous Media on the Performance of the Cathode of a PEM Fuel Cell.....</b>	<b>82</b>
4.1 Background.....	82
4.2 Capillary Functions.....	84
4.3 Model Development.....	92
4.3.1 Assumptions.....	93
4.3.2 Governing Equations.....	94
4.3.3 Boundary Equations.....	98
4.4 Results and Discussion.....	104
4.5 Conclusions.....	116
4.6 References.....	117

<b>Chapter 5 Modeling the Effects of the Micro-Porous Layer on the Net Water Transport Rate Across the Membrane in a PEM Fuel Cell.....</b>	<b>123</b>
5.1 Introduction.....	123
5.2 Model Development.....	129
5.2.1 Modeled Domain.....	129
5.2.2 Governing Equations.....	130
5.2.3 Boundary Conditions.....	133
5.2.4 Parameters and Correlations Used in the Simulation.....	137
5.3 Results and Discussion.....	138
5.3.1 With and Without MPL.....	138
5.3.2 Capillary Effect of the MPL.....	148
5.3.3 Preferred Combination of the GDL, MPL and CL.....	154
5.4 Conclusions.....	161
5.5 References.....	162
<b>Chapter 6 A Modeling Study of the Effects of Anode Porous Layer on the Performance of a PEM Fuel Cell.....</b>	<b>168</b>
6.1 Introduction.....	168
6.2 Model Development.....	169
6.2.1 Modeled Domain.....	169

6.2.2 Governing Equations.....	169
6.2.3 Boundary Conditions.....	171
6.2.4 Capillary Curves.....	173
6.2.5 Parameters Used in the Simulation.....	175
6.3 Results and Discussion.....	176
6.4 Conclusions.....	183
6.5 References.....	184
<b>Chapter 7 Conclusions and Recommendations.....</b>	<b>186</b>
7.1 Conclusions.....	186
7.1.1 Experimental.....	186
7.1.2 Modeling.....	188
7.2 Recommendations.....	190
7.2.1 Experimental.....	190
7.2.2 Modeling.....	192
7.3 Contributions to This Area.....	193
7.3.1 Direct Contributions.....	193
7.3.2 Indirect Contributions.....	194
7.4 References.....	195
<b>Appendix Experimental Data.....</b>	<b>198</b>

## List of Figures

<b>Figure 1.1</b>	Schematic of electrodes and charge flow of fuel cells.....	4
<b>Figure 1.2</b>	Schematic of components in a PEM fuel cell.....	9
<b>Figure 1.3</b>	Structure of Nafion.....	12
<b>Figure 1.4</b>	Polarization curve of a PEM fuel cell.....	18
<b>Figure 2.1</b>	Schematic of the relative permeability experiment.....	32
<b>Figure 2.2</b>	Neutron image (top view) of the relative permeability setup.....	34
<b>Figure 2.3</b>	Pressure drop and permeability of the material A1.....	38
<b>Figure 2.4</b>	Gas relative permeability of the material A1.....	40
<b>Figure 2.5</b>	Water displacement in a sample.....	40
<b>Figure 2.6</b>	Pressure drop and permeability of the material A3.....	42
<b>Figure 2.7</b>	Gas relative permeability of the material A3.....	43
<b>Figure 2.8</b>	Pressure drop and permeability of the material SGL 10CA.....	45
<b>Figure 2.9</b>	Liquid relative permeability of the material SGL 10CA.....	46
<b>Figure 2.10</b>	Pressure drop and permeability of the material Toray TGP-H-060 (30 %wt PTFE).....	47
<b>Figure 2.11</b>	Liquid relative permeability of the material Toray TGP-H-060 (30 %wt PTFE).....	48
<b>Figure 3.1</b>	Schematic of (a) a serpentine flow field, (b) an interdigitated flow field, (c)	

a cross-sectional view of the serpentine flow field, and (d) a cross-sectional view of the interdigitated flow field.  represents gas flowing out of the surface, and  represents gas flowing into the surface.....58

**Figure 3.2** Correlation between saturation level and permeability.....64

**Figure 3.3** Voltage, current density, and pressure drop in the test of sample B1. Stoichiometry of  $A/C=2/4$ , temperature of  $T_{\text{cell}}/T_A/T_C=70/70/70$  °C. A and C represent anode and cathode, respectively.....66

**Figure 3.4** Fuel cell performance, pressure drop, and saturation level of material B1. Stoichiometry of  $A/C=2/4$ , temperature of  $T_{\text{cell}}/T_A/T_C=70/70/70$  °C.....68

**Figure 3.5** Voltage, current density, and pressure drop in the test of sample B3. Stoichiometry of  $A/C=2/4$ , temperature of  $T_{\text{cell}}/T_A/T_C=70/70/70$  °C.....69

**Figure 3.6** Fuel cell performance, pressure drop, and saturation level of material B3. Stoichiometry of  $A/C=2/4$ , temperature of  $T_{\text{cell}}/T_A/T_C=70/70/70$  °C.....71

**Figure 3.7** Voltage, current density, and pressure drop in the test of sample B1. Stoichiometry of  $A/C=2/1.5$ , temperature of  $T_{\text{cell}}/T_A/T_C=70/70/70$  °C...73

**Figure 3.8** Fuel cell performance, pressure drop, and saturation level of material B1.

Stoichiometry of $A/C=2/1.5$ , temperature of $T_{\text{cell}}/T_A/T_C=70/70/70$ °C.....	74
<b>Figure 3.9</b> Voltage, current density, and pressure drop in the test of sample B1. Stoichiometry of $A/C=2/1.5$ , temperature of $T_{\text{cell}}/T_A/T_C=70/50/50$ °C...	75
<b>Figure 3.10</b> Fuel cell performance, pressure drop, and saturation level of material B1. Stoichiometry of $A/C=2/1.5$ , temperature of $T_{\text{cell}}/T_A/T_C=70/50/50$ °C.....	76
<b>Figure 4.1</b> Comparison of capillary pressure of materials with different capillary properties.....	85
<b>Figure 4.2</b> Liquid saturation level jump condition at two materials with different wetting properties (by Clint D. Frye, an undergraduate student in our group).....	86
<b>Figure 4.3</b> Experimentally determined capillary pressure of a GDL (Toray 060) and a fitted capillary curve of a CL.....	88
<b>Figure 4.4</b> Adjusted capillary functions of CL.....	89
<b>Figure 4.5</b> Adjusted capillary functions of GDL.....	91
<b>Figure 4.6</b> Schematic diagram of the modeled domain.....	93
<b>Figure 4.7</b> Saturation level in GDL and CL for the base case with G1 and C1 at various cell voltages (refer to Fig. 4.3 and Table 4.1).....	105

<b>Figure 4.8</b> The effect of the CL capillary functions on the saturation levels in the GDL and CL at 0.6V (refer to Fig. 4.4 and Table 4.1).....	106
<b>Figure 4.9</b> Capillary diffusion coefficients for different CL capillary functions (refer to Fig. 4.4 and Table 4.1).....	109
<b>Figure 4.10</b> The effects of the CL capillary pressure functions on the fuel cell performance (refer to Fig. 4.4 and Table 4.1).....	110
<b>Figure 4.11</b> The effect of the GDL capillary functions on the saturation levels in the GDL and CL at 0.6V (refer to Fig. 4.5 and Table 4.1).....	111
<b>Figure 4.12</b> Capillary diffusion coefficients for different GDL capillary functions (refer to Fig. 4.5 and Table 4.1).....	112
<b>Figure 4.13</b> The effects of the GDL capillary pressure functions on the fuel cell performance (refer to Fig. 4.5 and Table 4.1).....	113
<b>Figure 5.1</b> SEM picture of an MPL.....	126
<b>Figure 5.2</b> Schematic diagram of the modeled domain.....	129
<b>Figure 5.3</b> Capillary curves used in the case with and without the MPL. The fitting parameters of $a_1$ , $a_2$ , $b$ , $c$ , and $d$ are -22.7, -16.2, -644.9, 0.58, -7.6 for G1, -30.0, -7.0, -9878.4, 0.3, -4000.0 for M1, and -45.0, -8.0, 5000.0, 0.78, -1106.56 for C1, respectively.....	139
<b>Figure 5.4</b> (a) Liquid water saturation level, and (b) liquid pressure at 0.6V. G1, M1,	

and C1 were used in the case with the MPL; G1 and C1 were used in the case without the MPL (Refer to Fig. 5.3).....	141
<b>Figure 5.5</b> (a) Net liquid water fluxes, (b) liquid water fluxes of each component for the case without MPL, and (c) liquid water fluxes of each component for the case with MPL at 0.6V. G1, M1, and C1 were used in the case with the MPL; G1 and C1 were used in the case without the MPL (Refer to Fig. 5.3).....	144
<b>Figure 5.6</b> Water fluxes in the simulated domain at 0.6V. G1, M1, and C1 were used in the case with the MPL; G1 and C1 were used in the case without the MPL (Refer to Fig. 5.3).....	145
<b>Figure 5.7</b> Fuel cell performance. G1, M1, and C1 were used in the case with the MPL; G1 and C1 were used in the case without the MPL (Refer to Fig. 5.3).....	147
<b>Figure 5.8</b> Capillary curves used in the study of MPL capillary effect. The fitting parameters of a1, a2, b, c, and d are -30.0, -16.0, -9878.4, 0.1, -4000.0 for M2, -13.0, -10.5, -2000.0, 0.4, -500.0 for M3, respectively. G1, M1, and C1 are the same as those in Fig. 5.3.....	149
<b>Figure 5.9</b> MPL capillary effects on (a) the liquid water saturation level, (b) liquid pressure, and (c) liquid water flux at 0.6V (Refer to Fig.	



5.8).....	152
<b>Figure 5.10</b> MPL capillary effects on the water fluxes at 0.6V. Capillary curves of the GDL and CL were fixed to be G1 and C1, respectively (Refer to Fig. 5.8).....	153
<b>Figure 5.11</b> MPL capillary effects on the fuel cell performances (Refer to Fig. 5.8).....	154
<b>Figure 5.12</b> Capillary curves used in the preferred combinations. The fitting parameters of a1, a2, b, c, and d are -22.7, -10.0, -10000.0, 0.3, -2000.0, respectively, for G2. G1, M2, and C1 are the same as in Fig. 5.8.....	156
<b>Figure 5.13</b> (a) Liquid water saturation levels, (b) liquid pressure, and (c) liquid water fluxes at 0.6V (Refer to Fig. 5.12).....	159
<b>Figure 5.14</b> GDL effects on the fuel cell performances (Refer to Fig. 5.12).....	160
<b>Figure 6.1</b> Schematic diagram of the modeled domain.....	169
<b>Figure 6.2</b> Capillary curves used in the model.....	174
<b>Figure 6.3</b> Water needed to saturate a dry anode at 60 °C.....	177
<b>Figure 6.4</b> Distribution of (a) saturation levels, and (b) liquid water pressure in the modeled domain at 0.6 V.....	179
<b>Figure 6.5</b> Liquid water flux in the modeled domain at 0.6 V.....	180
<b>Figure 6.6</b> Effects of anode MPL on fuel cell performance.....	182

**Figure 6.7** Ionic potential in the modeled domain.....183

## List of Tables

<b>Table 1.1</b> Different types of fuel cells.....	7
<b>Table 1.2</b> $\Delta G_f$ , open circuit potential, and thermodynamic efficiency for PEM fuel cells.....	16
<b>Table 2.1</b> Properties of GDLs used in the experiment.....	29
<b>Table 2.2</b> Experimental conditions.....	36
<b>Table 3.1</b> Fuel cell operation conditions.....	61
<b>Table 3.2</b> Properties of gas transport media used in the experiment.....	62
<b>Table 4.1</b> Parameters of the capillary functions.....	92
<b>Table 4.2</b> Governing equations.....	94
<b>Table 4.3</b> Boundary conditions.....	99
<b>Table 4.4</b> Correlations used in the model.....	102
<b>Table 4.5</b> Parameters used in the model.....	103
<b>Table 4.6</b> Simulation conditions.....	104
<b>Table 4.7</b> Summary of the capillary effects.....	115
<b>Table 5.1</b> Governing equations.....	132
<b>Table 5.2</b> Boundary conditions.....	136
<b>Table 5.3</b> Parameters.....	137
<b>Table 5.4</b> Simulation conditions.....	138

<b>Table 6.1</b> Governing equations of the anode.....	170
<b>Table 6.2</b> Boundary conditions.....	173
<b>Table 6.3</b> Capillary functions.....	174
<b>Table 6.4</b> Parameters.....	175
<b>Table 6.5</b> Operation conditions.....	176
<b>Table A.1</b> Experimental data for Fig. 2.4.....	198
<b>Table A.2</b> Experimental data for Fig. 2.7.....	199
<b>Table A.3</b> Experimental data for Fig. 2.9.....	201
<b>Table A.4</b> Experimental data for Fig. 2.11.....	202
<b>Table A.5</b> Experimental data for Fig. 3.4.....	203
<b>Table A.6</b> Experimental data for Fig. 3.6.....	204
<b>Table A.7</b> Experimental data for Fig. 3.8.....	205
<b>Table A.8</b> Experimental data for Fig. 3.10.....	206

## List of Symbols

<i>a</i>	specific area ( $\text{cm}^2/\text{cm}^3$ )
AFC	alkaline fuel cell
BSL	base support layer
<i>C</i>	concentration ( $\text{mole}/\text{cm}^3$ )
CL	catalyst layer
<i>D</i>	diffusion coefficient ( $\text{cm}^2/\text{s}$ )
<i>F</i>	Faraday constant (coulomb/mole)
GDL	gas diffusion layer
<i>H</i>	Henry's constant ( $\text{atm cm}^3/\text{mole}$ )
HOR	hydrogen oxidation reaction
<i>i</i>	current density ( $\text{A}/\text{cm}^2$ )
<i>k</i>	conductivity ( $1/(\text{ohm} \cdot \text{cm})$ )
<i>K</i>	permeability ( $\text{cm}^2$ )
<i>m</i>	Catalyst loading
<i>M</i>	molecular weight ( $\text{g}/\text{mole}$ )
MCFC	molten carbonate fuel cell
MEA	membrane electrode assembly

MPL	micro-porous layer
$n$	electro-osmotic drag coefficient
$N$	flux ( mole/(s · cm <sup>2</sup> ) )
OCV	open circuit voltage
ORR	oxygen reduction reaction
$p$	pressure (Pa)
PAFC	phosphoric acid fuel cell
PEM	proton exchange membrane
PEMFC	proton exchange membrane fuel cell
PTFE	polytetrafluoroethylene
$R_{O_2}$	reaction rate ( mole/(s · cm <sup>3</sup> ) )
$R_w^c$	Phase change reaction rate ( mole/(s · cm <sup>3</sup> ) )
$s$	saturation level
SOFC	solid oxide fuel cell
T	temperature (K)

### **Greek and Roman letters**

$\delta$	thickness (cm)
$\varepsilon$	porosity

$\eta$	fuel cell maximum efficiency
$\lambda$	water content in Nafion
$\mu$	viscosity ( Pa · s )
$\xi$	effectiveness factor
$\rho$	density (g/cm <sup>3</sup> )
$\varphi$	modulus
$\phi$	ionic potential (V)

### **Subscripts and Superscripts**

agg	agglomerate
c	capillary
eff	effective
f	fixed charge site
g	gas phase
l	liquid
max	maximum
MEM	membrane
N	Nafion phase
O <sub>2</sub>	oxygen

Pt	platinum
v	water vapor
w	liquid water



# Chapter 1

## Introduction

### 1.1 Fuel Cell Benefits

Fuel cells are devices that convert chemical energy stored in fuels directly into electricity, providing several benefits over other technologies. First is efficiency: fuel cells provide two to three times more efficient usage of the fuel than that of a heat engine. Because of the high efficiency, greenhouse gas emissions will be reduced by 50% when hydrocarbon materials, such as methanol, monoxide, and natural gas, are used as fuels. When fuels from renewable energy sources are used, nearly zero greenhouse gas emission is achievable. Fuel cells are scalable; single fuel cells can be stacked together to meet the desired power output requirement. They are also durable and able to withstand various operating conditions (various temperatures, pressures and stoichiometries). Fuel cells are silent, greatly reducing noise pollution as well as air pollution. For fuel cells operated at high temperatures, the waste heat can be used to heat water or living spaces. Other benefits include high reliability, multi-fuel capability and ease of maintenance.<sup>1</sup>

The efficiencies of heat engines are limited by the Carnot cycle. The highest efficiency of a heat engine is determined by the high temperature of the heat source

and the low temperature of the environment.

$$\eta_{\max} = \frac{T_1 - T_2}{T_1} \quad [1.1]$$

Eq. 1.1 is the efficiency of the Carnot cycle, where  $T_1$  is the temperature of the heat source (K), and  $T_2$  is the temperature of the environment (K). A car's engine only converts about 16% of the energy in gasoline to power used to turn the wheels, which is much lower than the Carnot efficiency.<sup>1</sup> Fuel cell vehicles have already proven much more efficient than similar internal combustion vehicles. Toyota has published their efficiency results, showing their conventional gasoline vehicle having a tank-to-wheel efficiency of only 16%, while their FCVH-4 running with hydrogen shows a 48% tank-to-wheel efficiency.<sup>1</sup>

Fuel cells will increase the US energy security by reducing the reliance of the US on imported fossil fuels. Fuel prices will become more stable and international tensions will reduce with lesser competition for limited fossil fuel resources. The US is dependent on imported oil for almost two-thirds of its energy consumption. The transportation sector consumes about two-thirds of the total oil consumed in the US and accounts for over one-third of the total energy use. In 2006, the US imported about 13 million barrels of oil per day, which cost about 300 billion dollars a year.<sup>2</sup> The greater efficiency realized by fuel cells means that there is enormous promise for their application to the transportation sector. However, fuel cell vehicles are still

extremely expensive to produce because the materials and labor costs remain high. With those issues properly addressed, adoption of fuel cells in transportation will be more realistic in the near future. Fuel cell vehicles have been in operation in a few major cities (such as Vancouver, Canada, and Chicago, Illinois) for several years for demonstration purposes.<sup>3</sup>

## 1.2 Fuel Cell Types

There are five major types of fuel cells, each with a different type of electrolyte.<sup>4</sup>

<sup>5</sup> Each type of fuel cell will be examined in detail below. Fig. 1.1 shows a schematic of the electrodes and charge flow in a fuel cell.

(1) Alkaline fuel cell (AFC)

The reaction at the anode in an AFC is



The reaction at the cathode is



Combining Eqs. 1.2 and 1.3 gives the following net reaction



The electrons pass through an outer load from the anode to the cathode to generate the electricity. The hydroxide ions move in the electrolyte from the cathode to the anode, where they combine with hydrogen, releasing liquid water and electrons.

This reaction must be carried out in a base solution since the hydroxide ions in the electrolyte are required in the electrode reactions. Sodium hydroxide and potassium hydroxide solutions are often used in an AFC because of their low cost. An AFC was successfully used on the Apollo spacecrafts that took men to the moon. A similar AFC system is used to provide electrical power in the current space shuttle fleet.

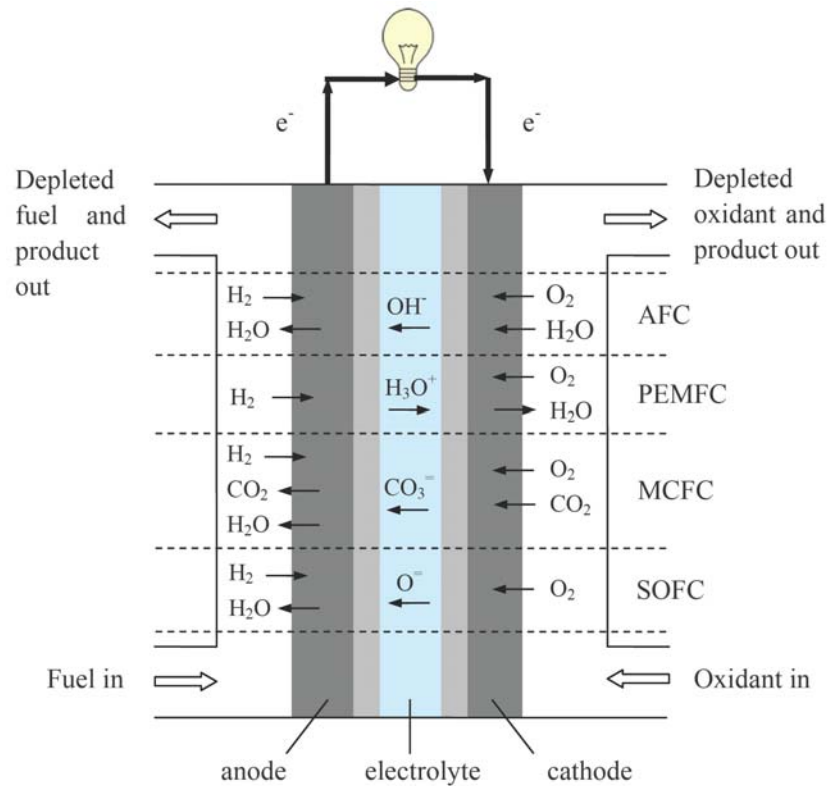


**Figure 1.1** Schematic of electrodes and charge flow of fuel cells.

(2) Proton exchange membrane fuel cell (PEMFC)

Proton exchange membrane fuel cells are also known as polymer electrolyte fuel

cells. A solid ion conductive polymer is used as the electrolyte, which also acts as an electrical separator of the anode and cathode. A commonly used membrane material is Nafion from DuPont. The reaction at the anode is



The reaction at the cathode is



The net reaction is



The Nafion membrane allows only protons to transport through it, while the electrons must travel through the outer load to generate electricity. When Eqs. 1.4 and 1.7 are compared, one sees that the net reaction of the AFC and PEMFC is the same. Their main differences are the type of electrolytes used in the fuel cell and the electrochemical reactions at the anode and cathode.

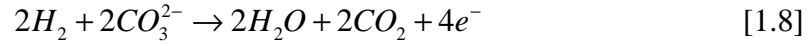
### (3) Phosphoric acid fuel cell (PAFC)

Phosphoric acid ( $H_3PO_4$ ) is used as the electrolyte for the transport medium of protons. The reactions in the anode and cathode are the same as those in Eqs. 1.5 and 1.6, respectively.

### (4) Molten carbonate fuel cell (MCFC)

In an MCFC fuel cell, a molten mixture of alkaline metal carbonate is used as

the electrolyte. When hydrogen is supplied as a fuel, the reaction at the anode is



The reaction at the cathode is



The net reaction is



Eq. 1.10 shows that carbon dioxide is consumed at the cathode side and released at the anode side. The negatively charged ion,  $CO_3^{2-}$ , passes through the electrolyte from the cathode to the anode.

#### (5) Solid oxide fuel cell (SOFC)

Similar to the MCFCs, a negatively charged ion,  $O^-$ , passes through the electrolyte from the cathode to the anode in a SOFC. However, the two differ in the type of electrolyte used and the reactions occurring at the electrodes. Instead of a molten electrolyte as in the MCFC, the electrolyte in a SOFC is a solid. When hydrogen is supplied as a fuel, the reaction at the anode side is



The reaction at the cathode is



The net reaction is

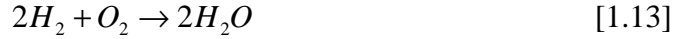


Table 1.1 summarizes the different types of fuel cells. The differences between them include the form of the electrolyte, the range of the operating temperature, and the type of the catalyst. At high temperatures, a fast reaction rate can be achieved without the use of a noble catalyst. On the contrary, at low temperatures, as in a PEMFC and PAFC, a noble catalyst like platinum is required to achieve fast reaction rates.

**Table 1.1** Different types of fuel cells.<sup>5,6</sup>

Fuel cell type	Electrolyte (mobile ion)	Operating temperature, °C	Catalyst Anode/Cathode
Alkaline (AFC)	KOH (OH <sup>-</sup> )	50 - 200	Pt/Pt or Ni/NiO
Proton exchange membrane (PEMFC)	Nafion (H <sup>+</sup> )	< 100	Pt/Pt or Pt-Ru/Pt
Phosphoric acid (PAFC)	Phosphoric acid (H <sup>+</sup> )	~ 200	Pt/Pt
Molten carbonate (MCFC)	Li-K or Li-Na carbonate (CO <sub>3</sub> <sup>2-</sup> )	~ 650	Ni-Cr/Lithiated NiO
Solid oxide (SOFC)	YSZ (ZrO <sub>2</sub> -Y <sub>2</sub> O <sub>3</sub> ) (O <sup>2-</sup> )	500 - 1000	Ni-YSZ/LaMnO <sub>3</sub> -Sr

### 1.3 PEM Fuel Cell Components and Transport

The proton exchange membrane (PEM) fuel cell is considered one of the most promising energy conversion devices for applications such as portable electronic

devices and automobiles in the near future. Fig. 1.2 shows the components in a PEM fuel cell. The cathode side includes a gas diffusion layer (GDL) and a catalyst layer (CL). The anode side has the same components as the cathode. The membrane made of Nafion separates the anode and cathode.

**Flow Plate:** The flow plate, usually made of carbon or graphite, provides the flow path for the reactants and serves as an electrical current collector. Carbon is superior to other metals as a current collector since metals are prone to corrosion, which can introduce metallic ion contaminants to the catalyst layers and membrane. However, the carbon plate is brittle and difficult to machine, which poses a challenge in its application.



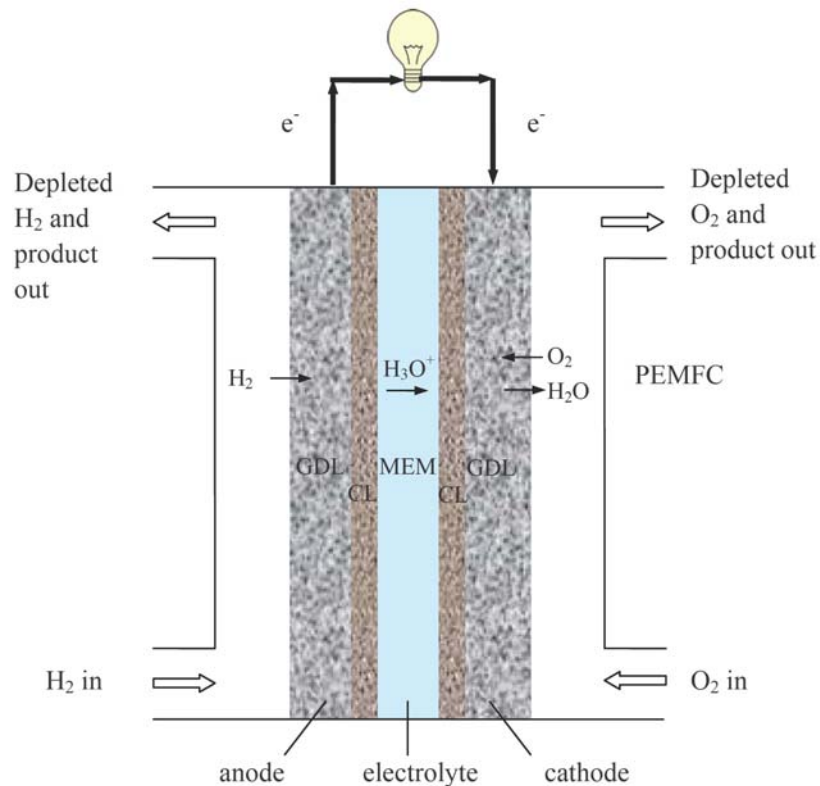


**Figure 1.2** Schematic of components in a PEM fuel cell.

**Gas Diffusion Layer:** The GDL provides the transport path for the reactants and the electrons to and from the CL in the anode and cathode. There are two kinds of GDLs: carbon paper and carbon cloth. Carbon paper is commonly used in fuel cells because of its simple manufacturing process. Commercially available GDLs are primarily produced by SGL Group and Toray Industries, Inc. The GDLs from Toray have lower porosity and are denser than those from SGL Group.

At the cathode, oxygen diffuses from the flow channel through the GDL to the CL, where it reacts with protons and electrons from the anode to produce water. The

product of liquid water moves through the GDL to the channel to be carried away by the air flow stream in the flow channel. At the anode, hydrogen flows through the GDL to the CL, where it is oxidized to produce the electrons. The electrons produced in the anode flow through the anode GDL, outer load, and the cathode GDL to react in the cathode CL. Finally, in addition to providing transport paths to the reactants, products, and electrons, the GDL also provides mechanical support to the catalyst layer.

From the functions of the GDL, it is evident that the fuel cell performance can be improved by optimizing the properties of the GDL. The transport processes in the GDL must be considered systematically since they are inherently related. Although high porosity is preferred for reactant and product transport, its effects on electrical conductivity and mechanical strength should be taken into consideration.

In some cases, a bi-layer GDL is used to increase its hydrophobicity. To create a bi-layer GDL, a micro-porous layer (MPL) is applied onto one side of the macro porous gas diffusion layer using a paste consisting of carbon and a hydrophobic phase, such as polytetrafluoroethylene (PTFE), to increase its hydrophobicity. Details of how to make an MPL can be found in reference 7. The dense MPL works like a water barrier layer, preventing the liquid water generated at the cathode catalyst layer from flowing out of the cathode CL. As a result, the effect of flooding in the cathode is

alleviated. The functions of MPL will be discussed in further detail in Chapter 5.

**Catalyst Layer:** The catalyst layer is the power generating component of a PEM fuel cell. As seen in Eqs. 1.5, 1.6, and 1.7, protons and electrons are generated in the anode and consumed in the cathode. The electrons generated in the anode move through the anode CL, GDL, and outer load to the cathode GDL and CL. The protons generated in the anode move through the Nafion membrane to the cathode CL. Thus, the CL is a three-phase transport and reaction region, which includes the gas phase, liquid phase, and solid phase (for electrons and protons). The porous structure of the CL provides the transport path for the gas and liquid. In some cases, the void volume of a CL shows both hydrophobic and hydrophilic characteristics when a hydrophobic phase, such as PTFE, is added. The liquid phase will move through the hydrophilic path, and the gas phase will move through the hydrophobic path. The carbon and platinum provide the transport path for the electrons. A proton conductive phase, Nafion, is added to the CL to provide the transport path for the protons. Thus, it is essential to optimize the three phases (gas, liquid and solid) by adjusting the ratio of the carbon supported catalyst/Pt, Nafion and PTFE to achieve the optimal fuel cell performance.<sup>8</sup>

**Membrane:** The anode and the cathode are connected by a Nafion membrane, which has the following structure:

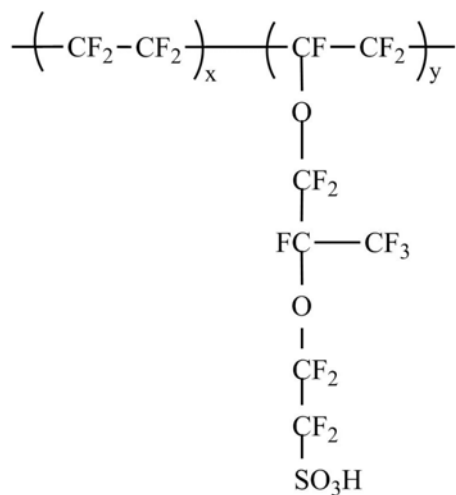


**Figure 1.3** Structure of Nafion.

Protons are transferred along the  $-\text{SO}_3\text{H}$  group, which is formed of  $\text{SO}_3^-$  ion and  $\text{H}^+$  ion. Nafion membranes are denoted with a letter N followed by a several digit number based on the molecular weight of the polymer and the thickness of the membrane. The first 2 digits represent the molecular weight divided by 100. The last one or two digits indicate the membrane thickness in the unit of mills (1 mill=1/1000 inch=0.0254 mm).<sup>4</sup> For example, Nafion N112 has the equivalent molecular weight of 1100 and thickness of 2 mills (0.0508 mm).

The backbone of Nafion ( $-\text{CF}_2-\text{CF}_2-$ ) is hydrophobic. However, the ionic group,  $-\text{SO}_3\text{H}$ , is hydrophilic, which attracts liquid water. The weight of dry Nafion can increase by as much as 50% wt when fully hydrated.<sup>5</sup> The conductivity of dry Nafion

is very low and increases with the amount of water absorbed.<sup>9</sup> Thus, saturated gas reactants are often used in a PEM fuel cell to keep the membrane hydrated and to provide high ionic conductivity. This requirement raises another issue of water management strategies in the PEM fuel cells: the flooded cathode and dry anode.

#### 1.4 PEM Fuel Cell Thermodynamics

For the reaction in a PEM fuel cell



the maximum energy available to do the external work is defined as the Gibbs free energy. The Gibbs free energy of the reaction is defined by the following equation

$$\Delta G_f^0 = G_{f,H_2O}^0 - G_{f,H_2}^0 + \frac{1}{2}G_{f,O_2}^0 \quad [1.15]$$

where  $\Delta G_f^0$  is the change of Gibbs free energy at the standard state (25°C, 1 atm partial pressure, 1 molal (1 mole/kg solvent)). Eq. 15 can be simplified further because  $G_{f,H_2}^0$  and  $G_{f,O_2}^0$  are zero.

$$\Delta G_f^0 = G_{f,H_2O}^0 \quad [1.16]$$

The charge involved in the reaction is

$$Charge = -2N \cdot e = -2F \text{ coulombs} \quad [1.17]$$

where N is the Avogadro number,  $N = 6.022 \times 10^{23} / \text{mole}$ ;  $e$  is the charge on one electron,  $e = 1.602 \times 10^{-19} \text{ coulombs}$ ; F is Faraday constant,  $F = 96485 \text{ coulombs}$ .

From Fig. 1.2, the electrical work consists of moving -2F charge from the anode

to the cathode, which can be calculated by

$$\text{Electrical work} = -2F \cdot E^0 \quad \text{joules} \quad [1.18]$$

where  $E^0$  is the reversible open circuit voltage at standard state. The reversible open circuit voltage of the PEM fuel cell can be derived from Eqs. 1.16 and 1.18.

$$\Delta G_f^0 = -2F \cdot E^0 \quad [1.19]$$

Thus,

$$E^0 = -\frac{\Delta G_f^0}{2F} \quad [1.20]$$

$\Delta G_f^0$  is a function of temperature and the state of the reactants and product. The activities of the reactant and the product affect the Gibbs free energy of the electrochemical reaction in the PEM fuel cell. From the thermodynamics arguments for a constant temperature, the Gibbs free energy of the Eq. 1.14 is expressed as

$$\Delta G_f = \Delta G_f^0 - RT \ln \frac{a_{H_2} \cdot a_{O_2}^{\frac{1}{2}}}{a_{H_2O}} \quad [1.21]$$

where  $\Delta G_f^0$  is the change of Gibbs free energy at the standard state;  $R$  is the ideal gas law constant (8.314 J/(mole·K));  $T$  is the temperature (K);  $a_{H_2}$ ,  $a_{O_2}$ , and  $a_{H_2O}$  are the activities of hydrogen, oxygen, and water, respectively.

Substitute Eq. 1.19 into Eq. 1.21, we have

$$-2F \cdot E = \Delta G_f^0 - RT \ln \frac{a_{H_2} \cdot a_{O_2}^{\frac{1}{2}}}{a_{H_2O}} \quad [1.22]$$

By rearranging Eq. 1.22, we obtain the following equation

$$\begin{aligned} E &= -\frac{\Delta G_f^0}{2F} + \frac{RT}{2F} \ln \frac{a_{H_2} \cdot a_{O_2}^{\frac{1}{2}}}{a_{H_2O}} \\ &= E^0 + \frac{RT}{2F} \ln \frac{a_{H_2} \cdot a_{O_2}^{\frac{1}{2}}}{a_{H_2O}} \end{aligned} \quad [1.23]$$

where  $E^0$  is the fuel cell potential at the standard state. Eq. 1.23 is called Nernst equation, which describes the effect of the activities of the reactants and product on the fuel cell potential. Note that this equation cannot be used to calculate the temperature dependence of the thermodynamic potential. Only the effect of the activities of the reactants and the products can be predicted by Eq. 1.23.

Fuel cell efficiency is defined as the ratio of electrical energy to the heat that would be produced by burning the fuel. The maximum electrical energy available is equal to the reversible energy that the fuel can supply, which is the Gibbs free energy, so

$$\eta_{\max} = \frac{\Delta G_f}{\Delta H_f} \times 100\% \quad [1.24]$$

$\eta_{\max}$  in Eq. 1.24 is also called the thermodynamic efficiency. However, values of  $\Delta H_f$  change with the state of the water in the electrochemical reaction. When water is in the form of gas and liquid state

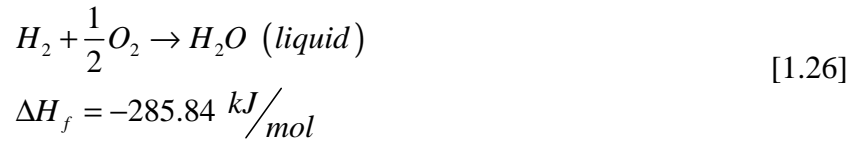
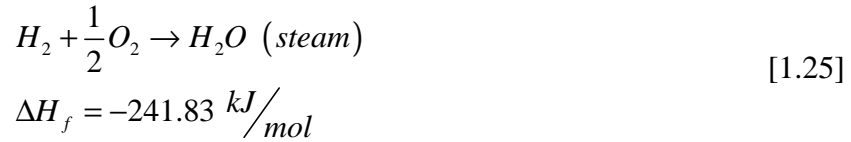


Table 1.2 summarizes the  $\Delta G_f$ , open circuit voltage (OCV), and thermodynamic efficiency based on the liquid state of the water product.

**Table 1.2**  $\Delta G_f$ , open circuit potential, and thermodynamic efficiency for PEM fuel cells.<sup>5</sup>

Form of water product	Temperature, °C	$\Delta G_f$ , kJ/mol	OCV, V	Thermodynamic efficiency, %
Liquid	25	-237.2	1.23	83
Liquid	80	-228.2	1.18	80
Gas	100	-225.2	1.17	79

## 1.5 PEM Fuel Cell Performance

Fig. 1.4 shows a typical polarization curve of a PEM fuel cell. The Nafion membrane is designed to be nonconductive of electrons and impermeable to gases. However, a very small amount of hydrogen can penetrate the membrane from the anode to the cathode to react with oxygen directly. This amount of hydrogen reactant is wasted without doing external work, leading to OCV loss.

The activation loss is caused by the slow electrochemical reactions on the



surface of the electrodes. In a PEM fuel cell, the cathode oxygen reduction reaction (ORR) is the main source of activation loss. The kinetic loss can be reduced by raising the temperature, using more active catalysts, and increasing the active catalyst surface.

The ohmic loss is caused by the resistance of the transport of ions and electrons in the electrodes of the PEM fuel cell. The magnitude of ohmic drop is proportional to the current as expressed in the following equation

$$V = IR_{ohm} \quad [1.27]$$

where the  $V$  is the potential,  $I$  is the current, and  $R_{ohm}$  is the resistance.

The mass transport loss is caused by reactant depletion. In a PEM fuel cell, water flooding at the cathode side often causes the mass transport limitation by blocking the gas transport path of the reactants. If convective flow through the electrode could be created, it would reduce the mass transport loss by providing higher concentrations of the reactants and alleviating the flooding effect in the PEM fuel cell. Consequently, gas flow field design is also an important aspect in a PEM fuel cell.

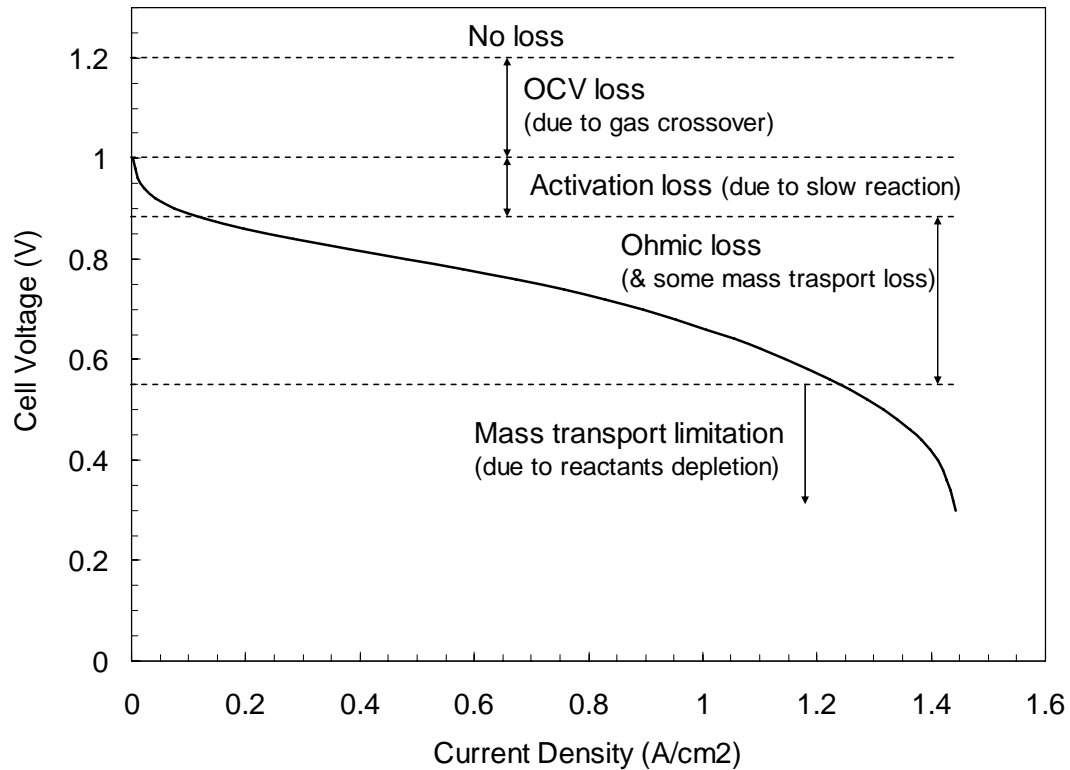


**Figure 1.4** Polarization curve of a PEM fuel cell.

## 1.6 Motivation and Objectives

PEM fuel cells depend on proper water management to obtain high power density and energy efficiency. During operation, as a result of the electro-osmotic effect the membrane at the anode side tends to be dry. Consequently, to avoid anode dehydration, water is added to the anode gas stream in the form of water vapor to compensate for the amount lost to the cathode by electro-osmosis. Meanwhile, at the cathode the opposite problem occurs. Liquid water in the cathode of a PEM fuel cell is generated from three sources: 1) liquid water dragged by electro-osmosis from the

anode to the cathode, 2) oxygen reduction reaction, and 3) condensation when a temperature gradient exists. When the water generated at the cathode by these three processes is not properly removed, its accumulation leads to poor fuel cell performance by blocking the gas pores used for oxygen gas transport and forming an additional transport barrier over the reactive area.

When the operating temperature of a PEM fuel cell is below 100 °C, two-phase flow behavior of the gas phase and liquid phase has a significant impact on the PEM fuel cell performance since both liquid and gas phases exist simultaneously. First, in order to provide a transport path for the gaseous reactant, liquid water existing in the cathode side of a PEM fuel cell must be efficiently removed. Liquid water may form a thin liquid film on the catalyst layer acting as an additional barrier to the transport of the reactant gas to the catalyst active surface. Second, the membrane must be kept hydrated to decrease the ionic resistance. Water vapor saturated gases are often used to achieve this condition. Third, under certain circumstances the anode side could be flooded when excessive liquid water is transported from the cathode side to the anode side.

Two-phase flow properties of the porous media used in PEM fuel cells are important in fuel cell optimization and water management strategies. The permeability and capillary pressure curves reported in the literature vary greatly. The

absolute permeability varies between  $10^{-11} \text{ m}^2$  to  $10^{-13} \text{ m}^2$ .<sup>10-13</sup> The 3<sup>rd</sup>-order power correlation of the relative permeability developed for well sorted sands was often used in modeling.<sup>14</sup> The Leverett function developed for sands was used to simulate the capillary pressure of these porous media.<sup>15-19</sup> However, the porous media used in PEM fuel cells have different surface properties and geometrical structures from sands, which leads to inaccurate predictions of the performance of PEM fuel cells.

Quantifying the liquid saturation level in the GDL will be helpful for validating two-phase flow models and determining the liquid water's role in affecting fuel cell performance. The conventional water management approach of adding water (gas/liquid phase) to the anode side and removing water from the cathode side is a self-defeating process. Water management can be made more efficient in a PEM fuel cell by engineering the material properties of the porous media used in the membrane electrode assembly (MEA) to force liquid water in the cathode back to the anode to achieve zero-net-water-transport-across-the-membrane.<sup>20</sup> If this could be achieved, it would minimize or eliminate the need for anode gas humidification. Modeling two-phase transport in the PEM fuel cells can provide the strategies to optimize fuel cell performance. Information extracted from the modeling will be useful in predicting and directing the experimental work.

Thus, the first objective of this research was to measure the two-phase transport

properties of the porous media used in PEM fuel cells. Experimental measurement of the permeability, developed at the University of Kansas lab and validated using neutron imaging facility at the National Institute of Science and Technology (NIST), is presented in Chapter 2. Chapter 3 describes the experimental measurement of the liquid water saturation levels in the cathode side. The pressure drop in the interdigitated flow field indicates the liquid water content in the GDL. This pressure drop was recorded in the experiment to calculate the relative permeability. The liquid water saturation level was calculated from a correlation between the permeability and the saturation levels. In Chapter 4 the capillary pressure effect of the GDL and CL on the fuel cell performance is simulated by a two-phase flow model. The effect of the position, shape, and slope of the capillary curves on the liquid water saturation level and the fuel cell performance was investigated. Chapter 5 focuses on the effect of the MPL on the water management strategies to achieve the goal of zero-net-water-transport-across-the-membrane. And finally, a model including both the anode and cathode is presented in Chapter 6. The operating conditions and properties of the anode side were investigated to elucidate the role of the anode side in a PEM fuel cell.

## 1.7 References

1. [www.fuelcells.org](http://www.fuelcells.org). In 2009.
2. J. Yanes and R. Grosse, US Oil Import Dependence: Which Way out?, *Int. J. Energy Sect. Manage.*, 1 (2), 195, **2007**.
3. M. M. Mench, *Fuel cell engines*, John Wiley & Sons: Hoboken, N.J., p xi, 2008.
4. F. Barbir, *PEM Fuel Cells: Theory and Practice*, Elsevier Academic Press: Amsterdam ; Boston, p xv, 2005.
5. J. Larminie and A. Dicks, *Fuel Cell Systems Explained*, 2nd ed.; J. Wiley: Chichester, West Sussex, p xxii, 2003.
6. D. Natarajan, Experimental and Modeling Studies on the Spatiotemporal Current Density Distribution in a PEM Fuel Cell, Thesis (Ph.D.), University of Kansas, Chemical and Petroleum Engineering, 2004.
7. Z. Qi and A. Kaufman, Improvement of Water Management by a Microporous Sublayer for PEM Fuel Cells, *J. Power Sources*, 109 (1), 38, **2002**.
8. R. Friedmann and T. V. Nguyen, Optimization of the Cathode Catalyst Layer Composition Using a Novel 2-step Preparation Method, *ECS Trans.*, 16 (2), 2021, **2008**.
9. T. E. Springer, T. A. Zawodzinski and S. Gottesfeld, Polymer Electrolyte Fuel-Cell Model, *J. Electrochem. Soc.*, 138 (8), 2334, **1991**.

10. J. T. Gostick, M. W. Fowler, M. D. Pritzker, M. A. Ioannidis and L. M. Behra, In-Plane and Through-Plane Gas Permeability of Carbon Fiber Electrode Backing Layers, *J. Power Sources*, 162 (1), 228, **2006**.
11. V. Gurau, M. J. Bluemle, E. S. De Castro, Y.-M. Tsou, T. A. Zawodzinski Jr. and J. A. Mann Jr, Characterization of Transport Properties in Gas Diffusion Layers for Proton Exchange Membrane Fuel Cells 2. Absolute Permeability, *J. Power Sources*, 165 (2), 793, **2007**.
12. J. Ihonen, M. Mikkola and G. Lindbergh, Flooding of Gas Diffusion Backing in PEFCs - Physical and Electrochemical Characterization, *J. Electrochem. Soc.*, 151 (8), A1152, **2004**.
13. M. V. Williams, E. Begg, L. Bonville, H. R. Kunz and J. M. Fenton, Characterization of Gas Diffusion Layers for PEMFC, *J. Electrochem. Soc.*, 151 (8), A1173, **2004**.
14. M. Kaviany, *Principles of Heat Transfer in Porous Media*, 2nd ed.; Springer-Verlag: New York, p 708, 1995.
15. T. Berning and N. Djilali, A 3D, Multiphase, Multicomponent Model of the Cathode and Anode of a PEM Fuel Cell, *J. Electrochem. Soc.*, 150 (12), A1589, **2003**.
16. H. Meng and C. Y. Wang, Model of Two-Phase Flow and Flooding Dynamics in

- Polymer Electrolyte Fuel Cells, *J. Electrochem. Soc.*, 152 (9), A1733, **2005**.
17. U. Pasaogullari and C. Y. Wang, Liquid Water Transport in Gas Diffusion Layer of Polymer Electrolyte Fuel Cells, *J. Electrochem. Soc.*, 151 (3), A399, **2004**.
18. U. Pasaogullari and C. Y. Wang, Two-Phase Modeling and Flooding Prediction of Polymer Electrolyte Fuel Cells, *J. Electrochem. Soc.*, 152 (2), A380, **2005**.
19. Y. Wang, Porous-Media Flow Fields for Polymer Electrolyte Fuel Cells II. Analysis of Channel Two-Phase Flow, *J. Electrochem. Soc.*, 156 (10), B1134, **2009**.
20. T. V. Nguyen, Water Management by Material Design and Engineering for PEM Fuel Cells, *ECS Trans.*, 3 (1) (1), 1171, **2006**.



## **Chapter 2**

# **Experimental Study of Relative Permeability of Porous Media Used in PEM Fuel Cells**

### **2.1 Introduction**

Both the liquid and gas phases exist in the porous media of PEM fuel cells because these devices usually operate at low temperatures. Water management strategies need to be well balanced to achieve optimal fuel cell performance. Two-phase flow properties of porous media used in PEM fuel cells are important in fuel cell optimization and water management strategies. On the one hand, to improve the transport of gaseous reactant and liquid water to and from the CL, the liquid water in the cathode side of a PEM fuel cell must be efficiently removed. Liquid water may also form a thin film on the active catalyst layer, blocking the active sites from accessing the electrochemical reaction. On the other hand, a water vapor saturated cathode and anode are preferred to provide high ionic membrane conductivity. Last, when a cathode with correct level hydrophobicity is used, sufficient water could be forced from the cathode back to the anode by permeation and diffusion to overcome the effect of electro-osmosis.<sup>1</sup> Hydrophobicity in the cathode can be created by adding a hydrophobic material, such as PTFE, to the GDL, MPL and CL to help

remove the liquid water from the cathode.<sup>2, 3</sup> Better understanding of the transport properties of these porous media used in PEM fuel cells will lead to new strategies for water management. Of these transport properties, the gas and liquid permeability of the porous media used in PEM fuel cells are two of these important transport parameters.

In numerical simulations, the permeability in the form of linear correlation,<sup>4-6</sup> polynomial correlation,<sup>7, 8</sup> and function of multiple variables<sup>9</sup> was used to describe the two-phase flow in porous media. These correlations of relative permeability of gas and liquid phases were functions of saturation levels that have not been validated by experimental data.

Experimentally measured gas absolute permeability of macro-porous media used in PEM fuel cells ranges from  $4.4 \times 10^{-13} \text{ m}^2$  to  $5.0 \times 10^{-11} \text{ m}^2$  depending on the porous media tested in the experiment.<sup>10-13</sup> Since carbon fibers prefer to stay in a parallel direction, anisotropic properties are observed in the porous media used in PEM fuel cells. In-plane permeability is higher than through-plane permeability because of the geometrical layout of the carbon fibers. In a bi-layer GDL, a thin layer of dense MPL on the surface of the macro-porous substrate may cause a large decrease in the absolute permeability due to the small pores introduced by the MPL. PTFE content in the macro-porous substrate reduces the permeability by decreasing the pore sizes as

well as the surface morphology. However, Gurau *et al.*<sup>11</sup> showed that the permeability of the MPL increased with the PTFE content. Gurau *et al.* attributed this effect to the increased rigidity and intra-agglomerate pores of the MPL when the PTFE was added. Benziger *et al.*<sup>14</sup> measured liquid permeability by flowing liquid water through a porous medium, using a liquid water column to control the liquid pressure. However, the saturation levels corresponding to the liquid permeability had to be determined separately, which introduced great uncertainties to the measurements. The ex-situ determined saturation levels might be different than the in-situ saturation levels in Benziger *et al.*'s experiment because liquid water might have drained from the tested sample when the liquid pressure applied to the GDL was removed.

In recent years, neutron imaging has been applied successfully to determine liquid water content in PEM fuel cells.<sup>15-19</sup> With the improved resolution of neutron imaging, it is possible to map both in-plane and through-plane water distribution in an MEA and the flow fields of the cathode and anode. A better understanding of the liquid water distribution process inside the porous-media is valuable for better water management strategies in PEM fuel cells because the fuel cell performance is related to the liquid water saturation levels inside the electrodes of the fuel cell. Although neutron imaging has been used to measure the water content in a PEM fuel cell during operation, it had not been used for transport property measurement such as the

correlation between the gas and liquid phase permeability and liquid water saturation level.

This chapter focuses on the experimental study of the gas and liquid permeability of the porous media used in PEM fuel cells to determine the correlation between the gas and liquid permeability and liquid water saturation level. The gas permeability of two proprietary GDLs was measured by gravimetric analysis and neutron imaging. The liquid permeability of two commercially available GDLs was measured by neutron imaging. The obtained correlations were then used to determine the liquid water saturation levels in the cathode and anode GDLs during operation. This work will be discussed in Chapter 3. These correlations were also incorporated into fuel cell models to provide more accurate predictions of the water saturation levels in a PEM fuel cell.

## **2.2 Experimental**

### **2.2.1 Materials**

Four different kinds of GDLs were tested in this experiment. Two of them are proprietary GDLs that are not yet available on the market. The other two are commercially available GDLs from Toray Industries, Inc. and SGL Carbon Group. The properties of these four kinds of GDLs are summarized in Table 2.1. In this study, constant sample thickness was used by controlling the thickness of the metal washers

in the fixture. Homemade stainless steel washers were used to prevent the samples from being over-compressed. The uncompressed sample thickness was used in calculating the porosity and gas and liquid permeability.

**Table 2.1** Properties of GDLs used in the experiment.

<b>Material Type</b>	<b>Thickness (<math>\mu\text{m}</math>)</b>	<b>Porosity</b>	<b>PTFE Content (%wt)</b>
A1 (Proprietary GDL)	216	0.81	0
A3 (Proprietary GDL)	325	0.85	5
SGL-10CA (Carbon Group)	380	0.85	10
TGP-H-060 (Toray Industries, Inc.)	190	0.78	30

### 2.2.2 Gas Permeability

A homemade fixture was used to measure the gas permeability of the GDLs listed in Table 2.1. A schematic view of the permeability measurement setup is shown in Fig. 2.1. To prevent water loss by evaporation, the gas used in the experiment was pre-saturated with water vapor by passing it through a bottle filled with de-ionized water. The temperature in the bubbler bottle was set 1~2 °C higher than the ambient temperature. Gas permeability measured by both the gravimetric analysis and neutron imaging was carried out in this experiment.

The pressure drop was measured by an electronic pressure transducer (26PC Series, Honeywell) and recorded by a data acquisition system (Personal Daq System

by Omega Engineering). The pressure transducer had an operating pressure range of  $\pm 5$  Psi.

*Permeability by gravimetric analysis:* The gravimetric analysis involved measuring the weight of the dry sample before the experiment and the weight of the wet sample after the experiment. The saturation level was calculated based on the difference between the wet and dry samples. The corresponding permeability was calculated from the pressure drop across the sample. In the gravimetric method, each experiment generated a datum point because the sample inside the fixture had to be removed from the fixture to be weighed in a balance. The gravimetric permeability measurement consisted of the following steps:

- 1) Weigh the dry GDL to be tested (the dry weight of the sample is denoted by  $m_1$ ).
- 2) Pre-saturate a sample in de-ionized water at 80 °C for 1 hour followed by cooling down to ambient temperature. At 80 °C, the surface tension is sufficiently lowered to allow the sample, even when it is hydrophobic, to be saturated with liquid water. Once saturated, it was found that water would remain in the sample as it was cooled to ambient temperature.
- 3) Assemble the saturated sample in the fixture shown in Fig. 2.1.
- 4) Flow gas through the saturated sample and record the pressure drop,  $P$ .

5) Disassemble the fixture at the end of the experiment and weigh the sample to obtain the wet weight,  $m_2$ ;

6) Calculate the saturation level by

$$s = \frac{(m_2 - m_1) / \rho_{H_2O}}{\varepsilon V_{total}} \quad [2.1]$$

where  $\rho_{H_2O}$  is the liquid water density;  $\varepsilon$  is the porosity of the sample under compression; and  $V_{total}$  is the total volume of the sample under compression.

Gas permeability is calculated from Darcy's law.

$$\overline{k}_g = - \frac{v_g \mu_g}{\frac{\Delta P_g}{\Delta x_g}} \quad [2.2]$$

where  $v_g$  is the gas velocity;  $\mu_g$  is the gas viscosity;  $\overline{\Delta P}_g$  is the gas pressure drop;  $\Delta x_g$  is the gas traveling path length. The gas velocity is assumed to be constant because the pressure drop is low resulting from the small dimensions of the sample.

7) Repeat steps 1) to 6) with a different flow rate to obtain the permeability at a different saturation level.

Once the saturation level and permeability were calculated, a correlation between them was obtained. The gas flow rate was varied to obtain multiple data points. Higher gas flow rates led to lower saturation levels because of the higher shear

rates associated with the higher gas flow rates, and vice versa.

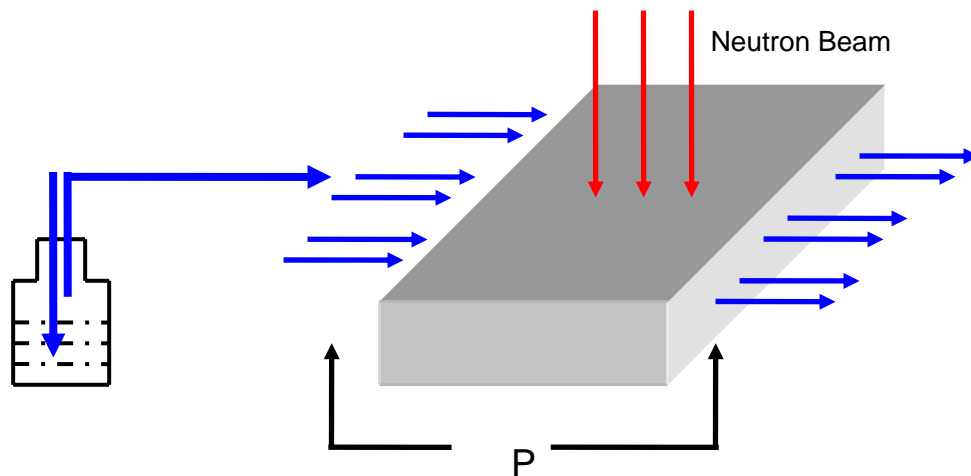


**Figure 2.1** Schematic of the relative permeability experiment.

*Permeability by neutron imaging:* The permeability of the porous medium tested in this experiment was calculated by Darcy's law using Eq. 2.2. Saturation levels of the porous medium were derived from the changes of the intensity of a neutron beam between the incident beam and the transmitted beam. Details of the mechanism by which the neutron imaging works were presented in reference 19. The image collecting rate is one picture per second and the resolution of the picture is 125 microns per pixel.

Fig. 2.1 illustrates how the in-situ liquid saturation levels in the sample were measured by neutron imaging during the experiment. Fig. 2.2 shows a neutron image



of the relative permeability fixture, in which a wet sample can be clearly seen. The procedures of the neutron imaging test are similar to those of the gravimetric analysis test. The only difference between these two methods lies in the method of determining the saturation levels in the wet sample. The procedure of the neutron imaging method is described as follows.

- 1) Pre-saturate a sample in de-ionized water at 80 °C for 1 hour followed by cooling down to ambient temperature.
- 2) Assemble the saturated sample in the fixture shown in Fig. 2.1.
- 3) Flow gas through the saturated sample, record pressure drop (  $P$  ), and acquire neutron images of the wet sample.
- 4) Flow dry air after the experiment to dry the sample.
- 5) Acquire neutron images of the dry sample. Images of the dry sample serve as references (backgrounds) to be subtracted from the neutron images of the wet sample to calculate the saturation levels.
- 6) Turn off the neutron beam and stop the experiment.

The saturation levels were calculated from the neutron images obtained in steps 3 and 5. The corresponding permeability was derived from the pressure drop across the gas flow path using Darcy's law shown in Eq. 2.2.

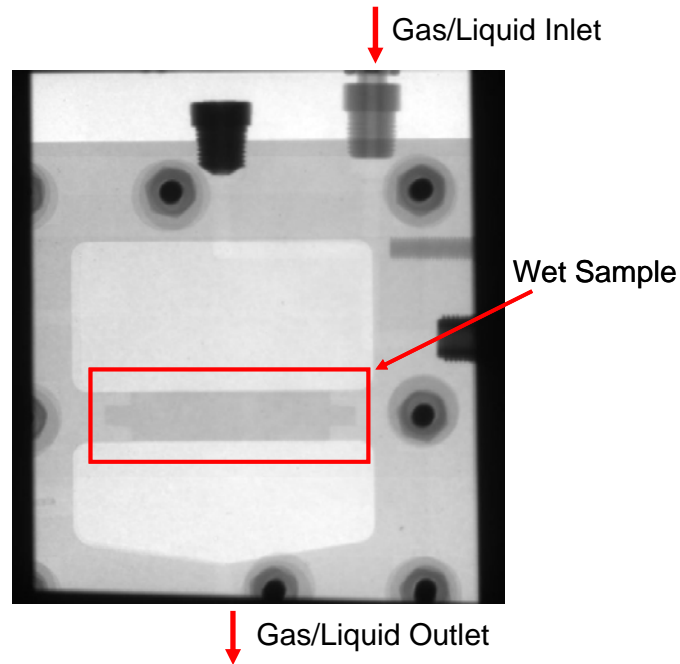


**Figure 2.2** Neutron image (top view) of the relative permeability setup.

### 2.2.3 Liquid Permeability

Neutron imaging technology as shown in Fig. 2.1 was used to measure the liquid permeability. The ex-situ permeability measurement showed an inconsistency of saturation levels because once the liquid pressure was removed, part of the liquid water may be repelled out of the sample as a result of the sample hydrophobic pore surface. Similar to gas permeability shown in Eq. 2.2, liquid permeability is calculated by

$$\bar{k}_l = - \frac{v_l \mu_l}{\frac{\Delta P_l}{\Delta x_l}} \quad [2.3]$$

where  $v_l$  is the liquid velocity;  $\mu_l$  is the liquid viscosity;  $\bar{\Delta P}_l$  is the liquid

pressure drop;  $\Delta x_l$  is the liquid traveling path. The liquid velocity is assumed to be constant for the same reason as stated earlier.

Contrary to the gas permeability measurement which started with a pre-saturated sample, the liquid permeability measurement starts with a dry sample. As the liquid displaces the gas phase when it flows through the sample, in-situ saturation levels are calculated from the change of the neutron beam intensities. The liquid permeability test includes three steps as follows.

- 1) Assemble a dry sample into the setup and acquire neutron images of the dry sample as reference or background images.

- 2) Flow liquid water through the sample as shown in Fig. 2.1, record liquid pressure drop, and acquire neutron images.

- 3) Turn off the neutron beam and stop the experiment at the end of the experiment.

The saturation levels and liquid permeability were calculated from the obtained neutron images and the pressure drop obtained in step 2. In order to measure the permeability at different saturation levels, liquid flow rate was adjusted during the experiment. A high saturation level is expected with a high liquid flow rate because at high liquid pressure more liquid water is expected to displace more void space in the porous medium.

The experimental conditions are summarized in Table 2.2. The sample size for the gas and liquid permeability measurement is 4 cm × 1 cm excluding the shoulders for sealing purposes. See Figs. 2.1 and 2.2. Gas and liquid traveling distance is equal to the width of the samples (1cm). The gas and liquid relative permeability experiment was conducted at ambient temperature. The outlet of the fixture is open to the air. Thus, the outlet pressure is assumed to be constant at 1 atm in this experiment.

**Table 2.2** Experimental conditions.

<b>Material Type</b>	<b>Fluid Traveling Distance (cm)</b>	<b>Flow Rate</b>
A1 (Proprietary GDL)	1	20 SCCM
A3 (Proprietary GDL)	1	60 SCCM
SGL-10CA (Carbon Group)	1	From 1.01 to 1.30 cm <sup>3</sup> /min
TGP-H-060 (Toray Industries, Inc.)	1	From 1.01 to 1.30 cm <sup>3</sup> /min

SCCM: standard cubic centimeter per minute

## 2.3 Results and Discussion

### 2.3.1 Gas Relative Permeability

Fig. 2.3 shows the gas phase pressure drop and the corresponding permeability of the material A1. At the beginning of the experiment, when the gas phase started to flow through the pre-saturated sample, sufficient pressure drop had to be created to displace the liquid phase. After the gas phase broke through the liquid phase, the gas

phase pressure drop decreased significantly. After 60 minutes, the saturation level in the sample was close to the residual saturation, which could not be displaced by the gas phase at this shear rate. At this stage, the gas phase pressure drop across the sample approached stability. The gas permeability changes corresponded to the change of the gas phase pressure drop as shown in Fig. 2.3. Since the experiment started with a pre-saturated sample, the gas permeability was very low at the beginning of the experiment. The measured permeability continuously increased as the liquid phase was displaced by the gas phase until the saturation level in the sample was close to the residual saturation at the end of 60 minutes. Pressure spikes observed after 60 minutes are likely due to the redistribution of the residual liquid water inside the porous GDL.

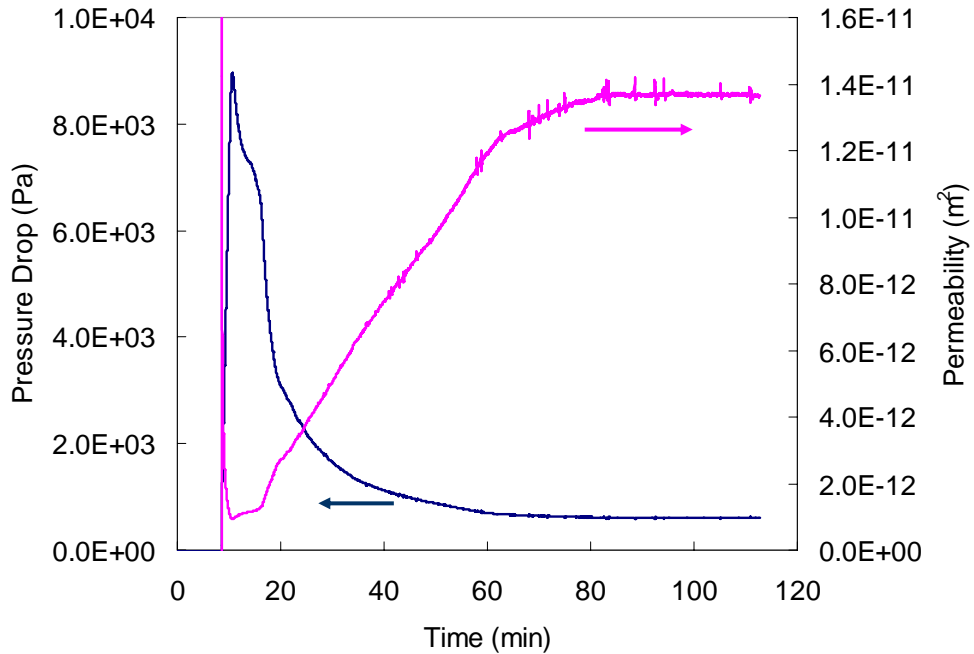


**Figure 2.3** Pressure drop and permeability of the material A1.

In the first 20 minutes, gas pressure drops greatly as shown in Fig. 2.3. The neutron images were averaged every 50 images (50 seconds) in the first 20 minutes. When the gas pressure approached steady state, the saturation levels became stable represented by stable pressure drop across the sample. Thus, after 20 minutes the neutron images were averaged every 200 images (200 seconds). From the grayness of these averaged density pictures and dry background pictures, liquid water saturation levels were derived based on the calibrated neutron beam parameters.

The relative permeability by gravimetric analysis and neutron imaging of material A1 were compared in Fig. 2.4. It was seen that at the same permeability, the

saturation level by the gravimetric analysis was higher than that of the neutron imaging. This discrepancy could be attributed to the fact that liquid water may be imbibed into the sample when the gas phase pressure was removed at the end of the gravimetric experiment. Neutron image showed that the liquid water displaced by the gas phase remained on the edge of the sample, as shown in Fig. 2.5, and could be re-imbibed into the sample again once the gas pressure was removed. As discussed in the previous part of this chapter, the liquid saturation level decreased drastically at the beginning of the experiment (high saturation level range), after which the saturation level dropped more gradually. During the process that the saturation levels dropped continuously, liquid water droplets could redistribute in a sample before they detached from the sample. Fig. 2.4 also showed that a 3<sup>rd</sup>-order power correlation in the form of<sup>20</sup>

$$k_g = k_0 (1-s)^3 \quad [2.4]$$

where  $k_0$  is the absolute permeability of a single phase, fitted the data of the gravimetric experiment a bit better than those of the neutron imaging. The 3<sup>rd</sup>-order power correlation was developed for nonconsolidated and well sorted sand. This shows that the 3<sup>rd</sup>-order power correlation cannot be used to predict the relative permeability of the sample A1 especially in the in-plan direction. Polynomial correlations of the gravimetric analysis and neutron imaging data was also shown in

Fig. 2.4.

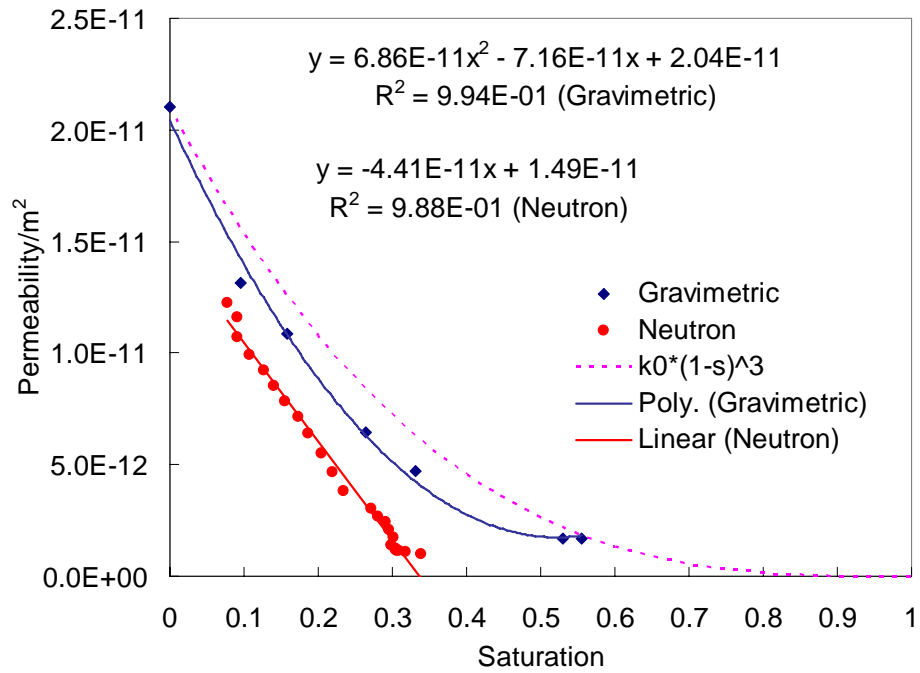


Figure 2.4 Gas relative permeability of the material A1.

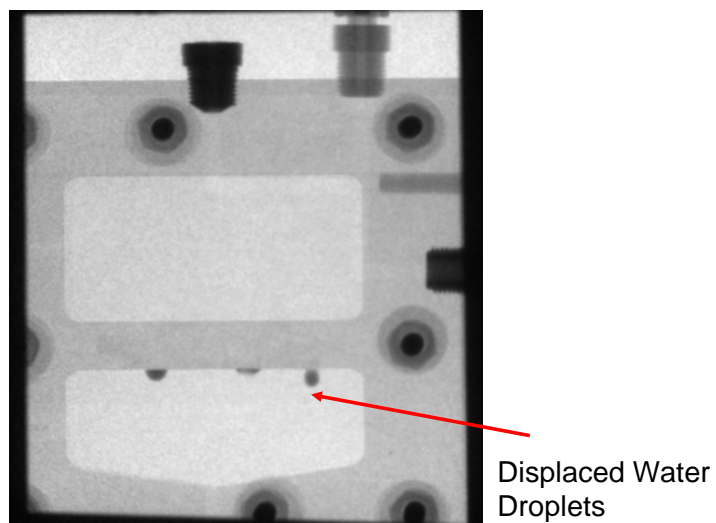
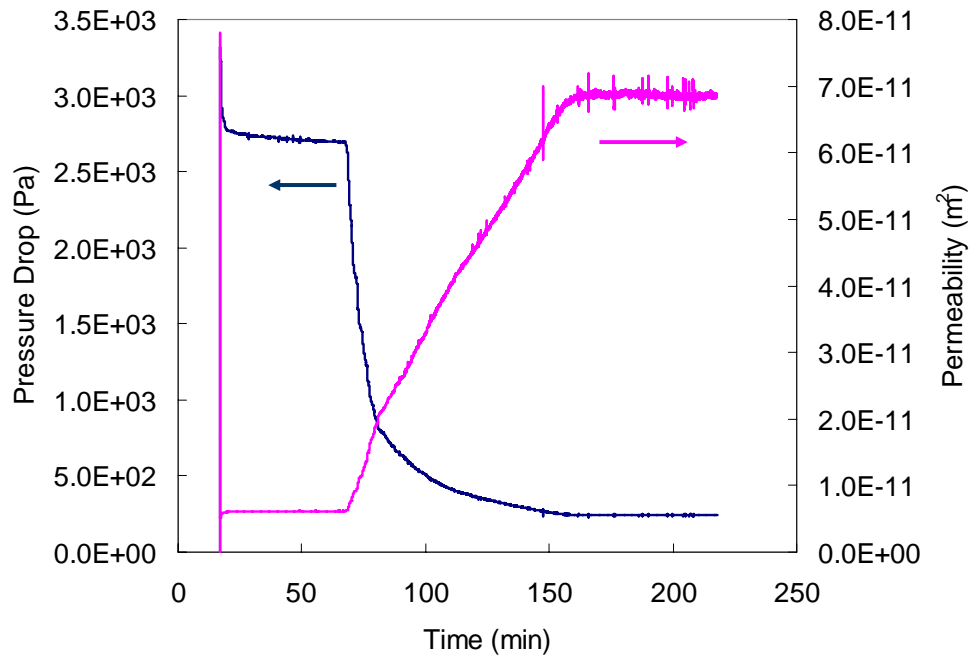


Figure 2.5 Water displacement in a sample.



The 3<sup>rd</sup>-order power correlation in Eq. 2.4 was developed for non-consolidated and well-sorted sand. The porous GDLs used in PEM fuel cells have different morphological and surface properties as a result of the carbon fibers which have a preferred in-plane layout. The special asymmetric property of the GDLs may explain the discrepancy between the 3<sup>rd</sup>-order power correlation and neutron imaging data.

The gas phase pressure drop and permeability of the material A3 were shown in Fig. 2.6. Similar to the phenomena observed in Fig. 2.3, sufficient gas pressure had to be created to break through the pre-saturated sample. A steep decrease of gas pressure drop and increase of gas permeability followed by a stable pressure and permeability were seen in Fig. 2.6. When gas started to flow through the sample, liquid water purged from the sample accumulated on the edge of the sample at the outlet as droplets. During this time, the pressure drop and permeability remained stable as seen in the 20-70 minute region in Fig. 2.6. Once the liquid droplets fell off the edge of the sample which allows more liquid water to be purged from the sample, the gas pressure drop began to decrease and continue until the saturation in the sample reached the residual level.



**Figure 2.6** Pressure drop and permeability of the material A3.

The saturation levels in material A3 were derived from the grayness of the density pictures. The density pictures were summarized and averaged in a similar way to that of material A1. When the pressure slope was steep, fewer neutron images were averaged to catch the change of saturation levels because the saturation levels drops greatly. When the pressure slope was low, more neutron images were averaged because the saturation levels were stable. In the liquid relative permeability measurement that follows, saturation levels were determined similarly based on the change of the liquid pressure drop.

Gas relative permeability of the material A3 is shown in Fig. 2.7. Gas

permeability by gravimetric analysis, neutron imaging, and 3<sup>rd</sup>-order power correlation had similar saturation levels in the range of 0 to 0.3, which showed that the 3<sup>rd</sup>-order power correlation provided a good fit to the experimental data in the low saturation level range for the material A3. Beyond the saturation level of 0.3, the gravimetric method showed higher saturation levels which could be attributed to the liquid water being re-imbibed into the sample when the gas pressured was terminated.

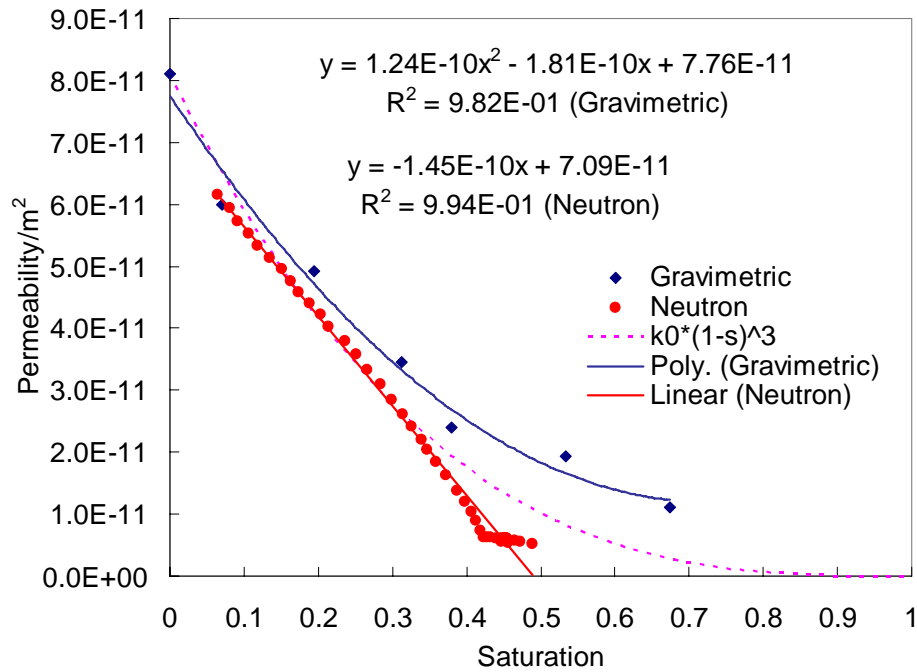
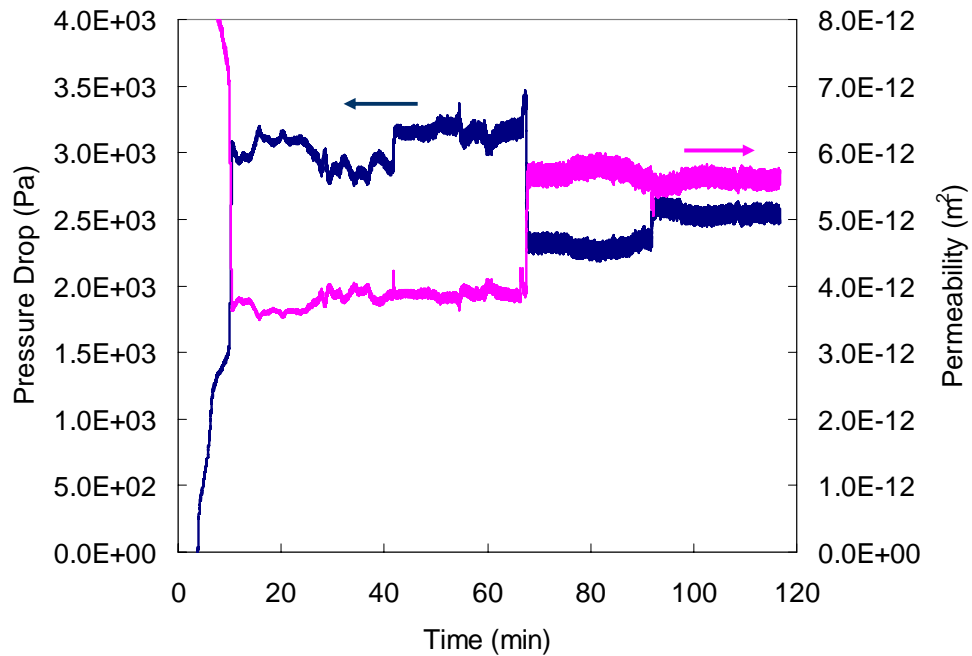


**Figure 2.7** Gas relative permeability of the material A3.

### 2.3.2 Liquid Relative Permeability

Multiple liquid water flow rates were used in measuring the liquid permeability

of the material SGL 10CA as shown in Fig. 2.8. Liquid water flow rate of 1.01 ml/min was first set from 0 to 41 min followed by the flow rate of 1.11 ml/min from 42 min to 66 min, 1.20 ml/min from 67 min to 92 min, and 1.30 ml/min from 93 min to 117 min. It was seen that liquid permeability was stable during the time range of 0 to 66 min because liquid water could not displace more gas phase in the porous material even when the liquid flow rate was increased from 1.01 ml/min to 1.11 ml/min. However, further increase of the liquid water flow rate from 1.11 ml/min to 1.20 ml/min resulted in a lower liquid pressure drop and higher liquid permeability as more gas phase was displaced under high liquid flow rate. A further increase of the liquid flow rate to 1.30 ml/min led to a higher pressure drop and minor change of permeability.



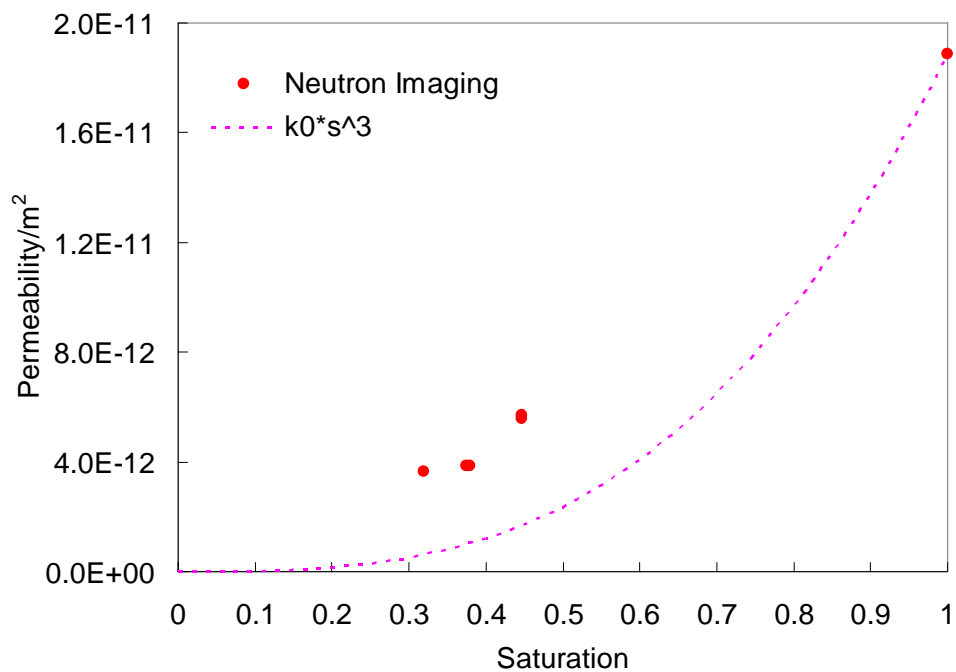
**Figure 2.8** Pressure drop and permeability of the material SGL 10CA.

Fig. 2.9 showed the liquid relative permeability by neutron imaging of the material SGL 10CA and a 3<sup>rd</sup>-order power correlation in the form of<sup>20</sup>

$$k_l = k_0 s^3 \quad [2.5]$$

The difficulty of obtaining the permeability at both high and low saturation levels was observed in this experiment. On one hand, gas phase may be trapped inside the material at high liquid water saturation levels as dead pockets, making it difficult to measure the permeability at a high saturation level. On the other hand, liquid saturation may have to reach a certain level before continuous liquid water flow across the sample could occur, making it difficult to measure the liquid permeability

at low liquid saturation level. Fig. 2.9 showed that there was a discrepancy between the permeability by neutron imaging and the 3<sup>rd</sup>-order power correlation, illustrating that the 3<sup>rd</sup>-order power correlation was inappropriate for SGL 10CA with its special porous geometry.



**Figure 2.9** Liquid relative permeability of the material SGL 10CA.

The liquid pressure drop and relative permeability of another porous material, Toray TGP-H-060 with 30 %wt PTFE, is shown in Fig. 2.10. Similar to the experiment of the SGL 10CA, liquid flow rates were 1.01 ml/min from 0 to 42 min, 1.11 ml/min from 43 min to 78 min, 1.20 ml/min from 79 min to 100 min, and 1.30

ml/min from 101 min to 127 min. It was seen that the liquid pressure drop fluctuated greatly with the change of liquid flow rate due to the redistribution of liquid water inside the sample. The liquid relative permeability increased slightly with the increase of the liquid flow rate since more gas phase was displaced with higher shear force created by the higher liquid flow rate. The stable liquid pressure drop observed may be attributed to the fact that the increased liquid saturation level at higher liquid flow rate resulted in higher permeability, which compensated for the increased liquid flow rate.

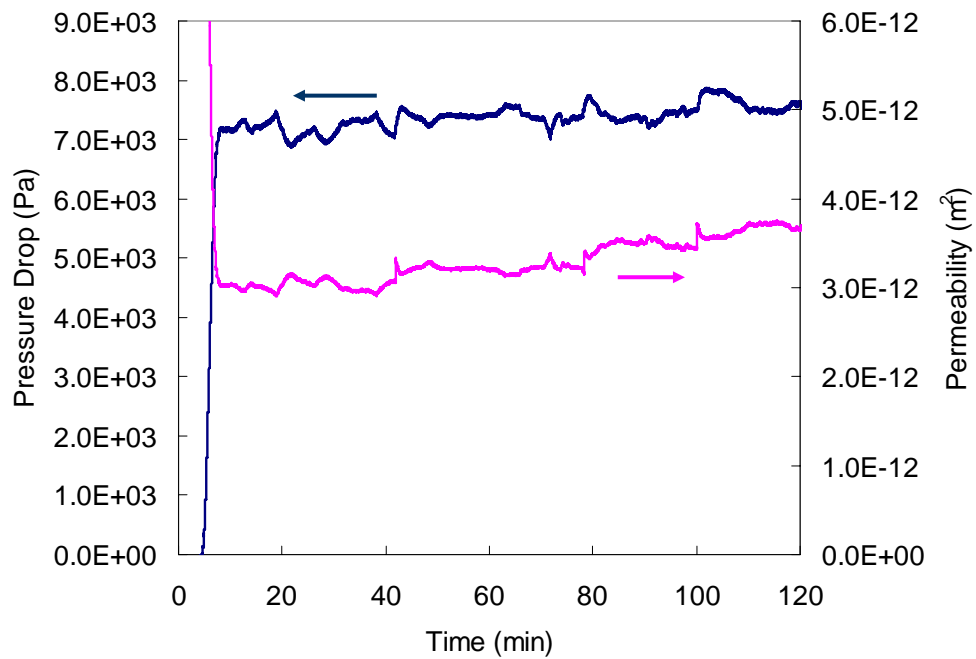


**Figure 2.10** Pressure drop and permeability of the material Toray TGP-H-060 (30 %wt PTFE).

Fig. 2.11 shows that liquid relative permeability by the neutron imaging can be predicted reasonably well by the 3<sup>rd</sup>-order power correlation. Liquid permeability increased with saturation level as the liquid flow rate increased. In the liquid relative permeability measurement, only a few data points in the saturation range of 0.5 to 0.8 could be obtained due to the difficulty explained earlier.

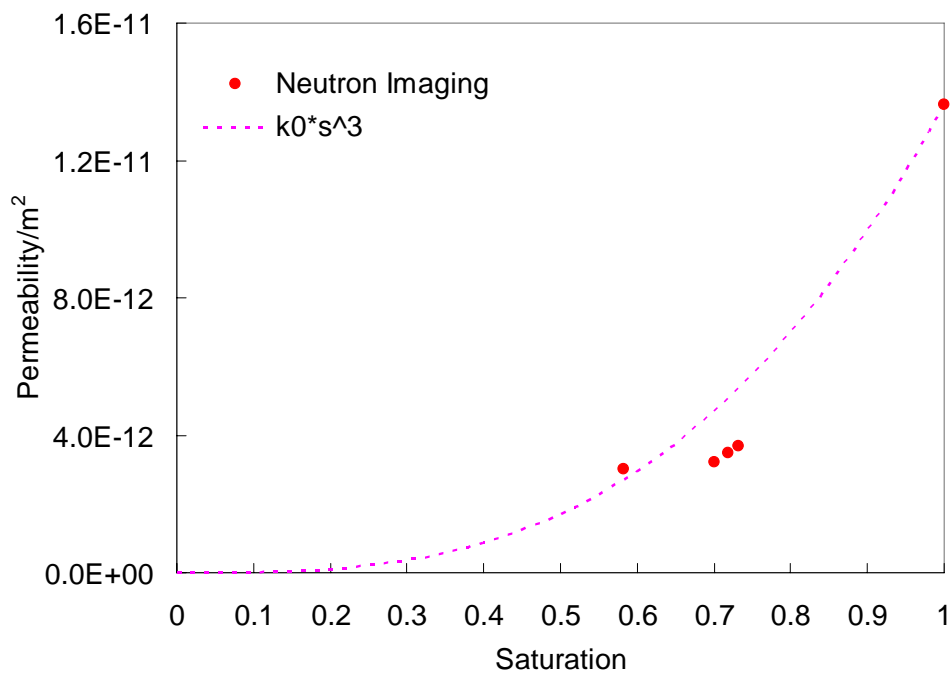


**Figure 2.11** Liquid relative permeability of the material Toray TGP-H-060 (30 %wt PTFE).



## 2.4 Conclusions

This chapter investigated gas and liquid relative permeability of porous GDLs used in PEM fuel cells by gravimetric analysis and neutron imaging. Gas phase relative permeability of two proprietary GDLs showed that permeability obtained by the gravimetric analysis and neutron imaging showed good agreement at low saturation levels. Discrepancies between these two methods arose at high saturation levels and can be attributed to the re-imbibition of liquid water at the end of the experiment in the gravimetric method. Liquid relative permeability of two commercially available GDLs showed that permeability increased with the liquid flow rate, resulting from the increase of saturation levels in the porous materials at high liquid flow rate. The impact of the liquid flow rate on the liquid pressure drop and permeability was insignificant, which may be resulted from the small change of the liquid flow rate used in this experiment. Due to dead air pockets in the porous GDLs and a certain liquid saturation level needed for the liquid to penetrate through the GDLs, liquid relative permeability was difficult to obtain at both high and low saturation levels. This study also showed that the 3<sup>rd</sup>-order power correlation of gas and liquid permeability was inappropriate for the porous media used in PEM fuel cells because those materials have a different structure from well sorted hydrophilic sands. The only exception was the liquid relative permeability of Toray TGP-H-060

with 30 %wt PTFE.

## 2.5 References

1. X. Wang and T. V. Nguyen, Modeling the Effects of the Micro-Porous Layer on the Net Water Transport Rate Across the Membrane in a PEM Fuel Cell, *J. Electrochem. Soc.*, in press, **2010**.
2. R. Friedmann and T. V. Nguyen, Optimization of the Cathode Catalyst Layer Composition Using a Novel 2-Step Preparation Method, *ECS Trans.*, 16 (2), 2021, **2008**.
3. M. F. Mathias, J. Roth, J. Fleming and W. Lehnert, Diffusion Media Materials and Characterisation. In *Handbook of Fuel Cells - Fundamentals, Technology and Applications*, W. Vielstich, H. A. Gasteiger and A. Lamm, Eds. John Wiley & Sons, Ltd.: Vol. 3: Fuel Cell Technology and Applications, pp 517, 2003.
4. W. He, J. S. Yi and T. V. Nguyen, Two-Phase Flow Model of the Cathode of PEM Fuel Cells Using Interdigitated Flow Fields, *AIChE J.*, 46 (10), 2053, **2000**.
5. G. Lin, W. He and T. V. Nguyen, Modeling Liquid Water Effects in the Gas Diffusion and Catalyst Layers of the Cathode of a PEM Fuel Cell, *J. Electrochem. Soc.*, 151 (12), A1999, **2004**.
6. D. Natarajan and T. V. Nguyen, A Two-Dimensional, Two-Phase, Multicomponent,

- Transient Model for the Cathode of a Proton Exchange Membrane Fuel Cell Using Conventional Gas Distributors, *J. Electrochem. Soc.*, 148 (12), A1324, **2001**.
7. U. Pasaogullari, C.-Y. Wang and K. S. Chen, Two-Phase Transport in Polymer Electrolyte Fuel Cells with Bilayer Cathode Gas Diffusion Media, *J. Electrochem. Soc.*, 152 (8), A1574, **2005**.
  8. Q. Ye and T. V. Nguyen, Three-Dimensional Simulation of Liquid Water Distribution in a PEMFC with Experimentally Measured Capillary Functions, *J. Electrochem. Soc.*, 154 (12), B1242, **2007**.
  9. A. Z. Weber, R. M. Darling and J. Newman, Modeling Two-Phase Behavior in PEFCs, *J. Electrochem. Soc.*, 151 (10), A1715, **2004**.
  10. J. T. Gostick, M. W. Fowler, M. D. Pritzker, M. A. Ioannidis and L. M. Behra, In-Plane and Through-Plane Gas Permeability of Carbon Fiber Electrode Backing Layers, *J. Power Sources*, 162 (1), 228, **2006**.
  11. V. Gurau, M. J. Bluemle, E. S. De Castro, Y.-M. Tsou, T. A. Zawodzinski Jr. and J. A. Mann Jr, Characterization of Transport Properties in Gas Diffusion Layers for Proton Exchange Membrane Fuel Cells 2. Absolute Permeability, *J. Power Sources*, 165 (2), 793, **2007**.
  12. J. Itonen, M. Mikkola and G. Lindbergh, Flooding of Gas Diffusion Backing in

- PEFCs - Physical and Electrochemical Characterization, *J. Electrochem. Soc.*, 151 (8), A1152, **2004**.
13. M. V. Williams, E. Begg, L. Bonville, H. R. Kunz and J. M. Fenton, Characterization of Gas Diffusion Layers for PEMFC, *J. Electrochem. Soc.*, 151 (8), A1173, **2004**.
14. J. Benziger, J. Nehlsen, D. Blackwell, T. Brennan and J. Itescu, Water Flow in the Gas Diffusion Layer of PEM Fuel Cells, *J. Membrane Sci.*, 261 (1-2), 98, **2005**.
15. A. B. Geiger, A. Tsukada, E. Lehmann, P. Vontobel, A. Wokaun and G. G. Scherer, In Situ Investigation of Two-Phase Flow Patterns in Flow Fields of PEFC's Using Neutron Radiography, *Fuel Cells*, 2 (2), 92, **2002**.
16. D. S. Hussey, D. L. Jacobson, M. Arif, J. P. Owejan, J. J. Gagliardo and T. A. Trabold, Neutron Images of the Through-Plane Water Distribution of an Operating PEM Fuel Cell, *J. Power Sources*, 172 (1), 225, **2007**.
17. T. Kim, J. Kim, C. Sim, S. Lee, M. Kaviany, S. Son and M. Kim, Experimental Approaches for Distribution and Behavior of Water in PEMFC under Flow Direction and Differential Pressure Using Neutron Imaging Technique, *Nucl. Instrum. Methods Phys. Res., Sect. A*, 600 (1), 325, **2009**.
18. T. Kim, J. Kim, C. Sim, S. Lee, Y. Son and M. Kim, Experimental Approaches for Water Discharge Characteristics in PEMFC Using Neutron Imaging Technique at

- Conrad, HMI, *Nucl. Eng. Technol.*, 41 (1), 135, **2009**.
19. R. Satija, D. L. Jacobson, M. Arif and S. A. Werner, In Situ Neutron Imaging Technique for Evaluation of Water Management Systems in Operating PEM Fuel Cells, *J. Power Sources*, 129 (2), 238, **2004**.
20. M. Kaviany, *Principles of Heat Transfer in Porous Media*, 2nd ed.; Springer-Verlag: New York, p 708, 1995.